Article

Fluid-Solid Coupling-Based Vibration Generation Mechanism of the Multiphase Vortex

Gaoan Zheng [1], Jilin Shi [2,*], Lin Li [3,4,5,*], Qihan Li [3], Zeheng Gu [3,5], Weixin Xu [3,5], Bin Lu [3,5] and Chengyan Wang [3,5]

1   College of Mechanical and Automotive Engineering, Zhejiang College of Water Resources and Hydropower, Hangzhou 310018, China
2   Linyi City Highway Business Development Center—Junan County Center, Linyi 276000, China
3   College of Mechanical Engineering, Zhejiang University of Technology, Hangzhou 310014, China
4   State Key Laboratory of Fluid Power and Mechatronic Systems, Zhejiang University, Hangzhou 310027, China
5   Key Laboratory of Special Purpose Equipment and Advanced Processing Technology, Ministry of Education & Zhejiang Province, Hangzhou 310014, China
*   Correspondence: shijilin@163.com (J.S.); linli@zjut.edu.cn (L.L.)

Abstract: Multiphase vortices are widely present in the metallurgical pouring processes, chemical material extraction, hydroelectric power plant energy conversion, and other engineering fields. Its critical state detection is of great significance in improving product yield and resource utilization. However, the multiphase vortex is a complex dynamics problem with highly nonlinear features, and its fluid-induced vibration-generation mechanism faces significant challenges. A fluid-solid coupling-based modeling method is proposed to explore mass transfer process with the vorticity distribution and vibration-generation mechanism. A vibration-processing method is utilized to discuss the four flow-state transition features. A fluid-induced vibration experiment platform is established to verify the numerical results. It is found that the proposed modeling method can better reveal the vibration-evolution regularities of the fluid-solid coupling process. The flow field has a maximum value in the complex water–oil–gas coupled flow process, and induces a pressure pulsation phenomenon, and its frequency amplitude is much larger than that of the water phase and water–oil two-phase flow states. In the critical generation state, the increasing amplitude and nonlinear step structure of high-frequency bands (45 Hz~50 Hz) and random pulse components can be used for the online detection of multiphase-coupling states.

Keywords: multiphase vortex; fluid-solid coupling; fluidic vibration; stochastic signal processing; metallurgical pouring process

1. Introduction

As a typical fluid flow pattern in industrial production processes, multiphase vortices often existed in significant engineering applications such as metallurgical casting and chemical material extraction [1–3]. The vortex suction process can suck surface fluid mediums and solid particles. Its gas–liquid suction effect will cause nonlinear shock vibration, resulting in many adverse effects on the industrial production process [4–6]. For example, in the process of steel flow refining, oxidizing agents and impurities are mixed to produce liquid steel slag and oxidizing impurities. As the steel flow flows out from the metallurgy vessel, the vortex induces intensive disturbance reaction and irregular load, affecting molten steel's purity and quality, and resulting in industrial accidents [7,8]. Moreover, the vortex entrainment phenomenon is an essential issue for safe production. The formed vortex core tends to reduce the reliability of the fuel system, and many bubbles can result in unstable combustion and high costs. To reduce the adverse effects caused by vortices, studying the fluid-induced vibration generation mechanism and taking effective vortex-suppression

measures to control the vortex-formation conditions are of great scientific value and broad application prospects.

In practical engineering applications, the multiphase vortex-pumping process forms a gaseous vortex core accompanied by complex physical phenomena, such as heat and mass transfer, energy exchange, and shock vibration [9–11]. Meanwhile, the vortex-formation process frequently occurs in thin-walled vessels with limited space. It is limited by extreme physical conditions such as high temperature and external interference. Video signals make it difficult to detect flow states inside flow channels, and the multiphase vortex-induced vibration-generation mechanism is challenging to reveal. Therefore, it is of great significance to study vibration-evolution mechanisms of multiphase vortex.

Academics have conducted numerous studies to address the issue of vortex-induced vibration creation. Kim discussed the vortex diffusion process and found that with the increase in the Reynolds number, the mass transfer rate between the flow area and vortex can be improved [12]. Ann simulated the gas–liquid vortex in the turbine operation and found that the two-phase vortex has a great influence on the inlet flow, resulting in an inhomogeneous pipe flow [13]. Takács performed a time-domain analysis of the two-phase vortex-induced vibration and found some vibration components in the experimental data [14]. Based on the fluid similarity principle, Wang studied the vortex-sucking slag phenomenon and found that the vortex was well suppressed and controlled at a blowing flow rate of 0.16 L/min [15]. Zhang used a wavelet algorithm to analyze the non-smooth vibrational data, and obtained the anomalous energy spectrum induced by two-phase vortex-sucking impurities [16].

From the above literature, it can be inferred that the current research on multiphase vortices mainly focuses on two-phase modeling, disturbance factors, and vibration features. The fluid-induced vibration mechanism in the multiphase vortex evolution is still unclear. Due to the complexity of the multiphase-coupling process, the dynamic characteristics of the fluid-induced vibration are highly nonlinear, which undoubtedly increases the difficulty of the vortex-induced vibration detection. Therefore, it is necessary to propose a fluid-solid coupling modeling method of the multiphase vortex to reveal the fluid-induced vibration mechanism.

This paper present a fluid-solid coupling-based multiphase vortex modeling method to explore fluid-induced vibration-evolution characteristics. A time/frequency signal processing method is combined to extract the vibration dynamics features and detect the critical vortex formation states. The related technical advancement is identified as follows. (1) A fluid-solid coupling model is conducted to acquire vibration-generation mechanism. (2) Explore the mass transfer process with the vorticity distribution characteristics. (3) Discuss the four flow-state transition features with the vibration-sensing method. (4) A fluid-induced vibration experiment platform is established to verify the numerical results. The relevant work can provide valuable references for theoretical studies on vortex formation mechanism, multiphase-coupling, and fluid-induced vibration, and is of universal significance for the fluid state identification, such as metallurgy pouring processes and pipeline transportation monitoring.

2. Mathematical Model and Solution Method

2.1. Mathematical Model

Multiphase vortex is a complex multiphase-fluid nonlinear-coupling problem, wherein the tracking of the multiphase fluids and the dynamic evolution process of the interphase interface are a research focus that needs attention. For the multiphase flow, the coupled level set and volume of the fluid model with the advantages of small interface curvature error and mass conservation are used to track with multiphase flow simulations [17–20].

The model defines the level set function as δ, denoting the characteristic distance to the interface. This value is negative at the upper fluid, zero at the interface, and positive at the lower fluid. The convective transport equation [21,22] is defined as

$$
\begin{cases}
\frac{\partial \delta}{\partial t} + (\mathbf{u}_m \cdot \nabla)\delta = 0 \\
\frac{\partial \gamma}{\partial t} + (\mathbf{u}_m \cdot \nabla)\gamma = 0
\end{cases} \tag{1}
$$

where $\mathbf{u}_m$ is the average velocity vector of the mixed fluid and t is the time. The normal vector $\mathbf{n}$ and the mean curvature κ are calculated for the gradient perpendicular.

$$
\mathbf{n} = \left.\frac{\nabla\delta}{|\nabla\delta|}\right|_{\delta=0} \quad \kappa = \nabla \cdot \mathbf{n} = \left.\nabla \cdot \frac{\nabla\delta}{\nabla\delta}\right|_{\delta=0} \tag{2}
$$

In multiphase flow calculations, the mixing density ρ_m and viscosity μ_m near the interface depend on the level set function. During the interface transition, the fluid physical parameters, such as density and viscosity, can be smoothed using the smoothing heaviside function.

$$
\begin{cases}
\rho_m(\varphi) = \rho_i[1 - H(\varphi)] + \rho_j H(\varphi) \\
\mu_m(\varphi) = \mu_i[1 - H(\varphi)] + \mu_j H(\varphi)
\end{cases} \tag{3}
$$

where the subscripts i and j denote the upper and lower fluids, and the smooth heaviside function is as follows.

$$
H(\delta) = \begin{cases}
1 & \delta > \eta \\
\frac{1}{2}\left[1 + \frac{\delta}{\eta} + \frac{1}{\pi}\sin\left(\frac{\pi\delta}{\eta}\right)\right] & |\delta| \leq \eta \\
0 & \delta < -\eta
\end{cases} \tag{4}
$$

where η is the simulated thickness of the interface, $\eta = 1.5\,b$ (the value of b is the grid space), and the model's liquid and gas phases are considered incompressible Newtonian fluids [21–23]. The continuity equation and Navier–Stokes equation [24,25] can be described as

$$
\frac{\partial \rho_m}{\partial t} + \nabla \cdot (\mathbf{u}_m \rho_m) = 0 \tag{5}
$$

$$
\frac{\partial}{\partial t}(\rho_m + \mathbf{V}_m) + \nabla \cdot (\rho_m V_m V_m) = -\nabla p + \nabla \cdot [\mu_m(\nabla \mathbf{V}_m + \nabla \mathbf{V}_m{}^T)] + \rho_m \mathbf{g} + \sigma\kappa\mathbf{n}\delta(\varphi) \tag{6}
$$

where ρ_m is the volume average density of the mixed fluids, p is the hydrostatic pressure, μ_m is the volume average viscosity of the mixed fluid, $\mathbf{g}$ is the acceleration of gravity, and $\sigma\kappa\mathbf{n}\beta(\delta)$ is the interfacial tension, where $\mathbf{n}$ is the interfacial normal vector, $\beta(\delta)$ is the surface function, and β is the surface tension coefficient.

2.2. Solid Model

The solid coupling model is a thin-walled cylindrical shell. As a single-point harmonic force is applied, its vibration must move concurrently in the axial, normal, and circumferential directions from the force point to the surface [26–29]. This paper uses the Flügge shell theory to set up a finite-length fluid-solid coupled dynamics model. Considering the propagation of the vibration wave along the shell axial direction, the displacement solutions of the Flügge equation with axial wave number [27] are obtained as follows:

$$
\begin{cases}
u_s = \sum\limits_{m=0}^{\infty}\sum\limits_{s=1}^{\infty} U_{ms}\cos(m\theta)\exp[i\omega t - ik_{ms}x] \\
v_s = \sum\limits_{m=0}^{\infty}\sum\limits_{s=1}^{\infty} V_{ms}\sin(m\theta)\exp[i\omega t - ik_{ms}x] \\
w_s = \sum\limits_{m=0}^{\infty}\sum\limits_{s=1}^{\infty} W_{ms}\cos(m\theta)\exp[i\omega t - ik_{ms}x]
\end{cases} \tag{7}
$$

where U_{ms}, V_{ms}, and W_{ms} are the displacement amplitudes of the shell components in the three directions of the column coordinates (x, θ, and r), m is the circumferential mode number, ω is the circular frequency, k_{ms} is the axial wave number, and the subscript s is the ordinal number of the axial wavenumber solution in the dispersion equation [29–31].

Assuming that the fluid is an ideal incompressible medium without viscosity, the fluctuation equation for the flow field in the column coordinate system is obtained as

$$\frac{1}{r}\frac{\partial}{\partial r}\left(r\frac{\partial p_s}{\partial r}\right) + \frac{1}{r^2}\frac{\partial^2 p_s}{\partial \theta^2} - \frac{1}{C_f^2}\frac{\partial^2 p_s}{\partial t^2} = 0 \tag{8}$$

where C_f is the wave velocity of the sound field. In this paper, the Helmholtz equation for the sound pressure field is solved by the variable separation method [32,33]. Considering the radiation and shell boundary coupling conditions, the sound pressure field satisfying the fluctuation equation [33] is as follows.

$$p_s = \sum_{m=0}^{\infty}\sum_{s=1}^{\infty} P_{ms}\cos(m\theta)Y_m(k_s^r r)\exp[i\omega t - ik_{ms}x] \tag{9}$$

where k_s^r denotes the radial wavenumber and may be determined via $(k_s^r)^2 = k_0^2 - k_{ms}^2$, $k_0 = \omega/C_f$ represents the free wave number of the fluids, P_{ms} represents amplitudes of acoustic pressure fields, and $Y_m(\tau)$ denotes the n-order Bessel functions [34,35]. At contact surfaces, fluid and shell radial displacements must match as follows:

$$-\frac{1}{i\omega\rho}\frac{\partial p_s}{\partial r}\bigg|_{r=R} = \frac{\partial w}{\partial t}\bigg|_{r=R} \tag{10}$$

The acoustic pressure can be calculated by substituting Equations (8) and (9) into Equation (10). The equations of motion of the coupled system can be solved by substituting Equations (7) and (9) into Equation (10). Due to random excitations and exhibit nonlinear characteristics, the axial cosine-distribution harmonic load [35] can be used to analyze the random excitation.

$$p(x,\theta,t) = F_x\cos(m\theta)\varphi(x)\exp[i\frac{\lambda}{R}x - i\omega t] \tag{11}$$

where F_x represents the force on the unit perimeter, and $\varphi(x)$ is the unit pulse function.

3. Fluid-Solid Coupling Numerical Model

3.1. Numerical Model

In order to track the critical transition state of multiphase vortex in real-time, a multiphase vortex numerical model based on the fluid-solid coupling is set up, as shown in Figure 1. The numerical model in the fluid domain mainly solves the continuity equation and turbulent kinetic energy equation to obtain the evolution law of the vortex flow field. The mesh quality has a significant impact on the accuracy of the transient calculation results. This section uses the Cooper algorithm [36,37] to mesh the model and accurately capture the dynamic coupling characteristics. The total number of hexahedral multi-block structured meshes is 335,460. The structured mesh is used to mesh the solid model, the total mesh number of the solid domain is 12,845, and the mesh quality is adjusted to the highest the calculation allows. The mesh division in Figure 1 shows that the model mesh division is more uniform, and the mesh near the drainpipe is relatively dense.
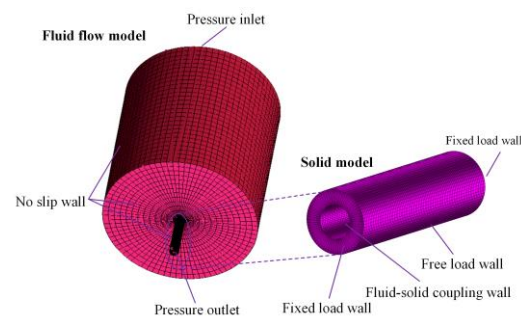
Figure 1. Fluid-solid coupling numerical model.

3.2. Boundary Conditions and Initial Conditions

To observe the multiphase vortex-formation process, the geometric characteristics of the vessel are shown in Table 1. The momentum equation solution of the flow field needs to determine the boundary conditions of the fluid domain, and reasonable and realistic boundary conditions can obtain an accurate numerical solution. In Figure 1, the container inlet is the air phase and set as pressure inlet boundary conditions, and the outlet boundary is set as the pressure outlet. Assuming that the velocity or relative velocity at the initial fluid wall is zero, the wall conditions are defined as no-slip wall boundary conditions. The basic parameters of the multiphase flow medium are shown in Table 2. Here, the initial tangential velocity and gravitational acceleration act on the flow field. In the solid model (Figure 1), the upper and lower wall surfaces are fixed-load surfaces, and the inner wall surface is coupled with the flow field model's wall surface, forming a fluid-solid coupling surface. It can realize the real-time interaction between the flow field and the solid field data, and the outer wall surface of the shell is the free-load surface. The PC plastic (elastic modulus 2.4×10^3 Mpa) is selected as the model material to discuss vibration characteristics.

Table 1. Boundary conditions of the numerical model.

Item	Parameter
Gravity magnitude/(N)	9.81
Gas zone height/(m)	0.3
Oil zone height/(m)	0.05
Water zone height/(m)	0.2
Vessel height/(m)	0.55
Vessel diameter/(m)	0.5
Pipe length/(m)	0.15
Pipe diameter/(m)	0.022

Table 2. Physical parameters of fluid mediums.

Medium	Kinetic Viscosity/ $(m^2 \cdot s^{-1})$	Dynamic Viscosity/ $(Pa \cdot s)$	Density/ $(kg \cdot m^{-3})$
Oil	1.01×10^{-6}	2.4×10^{-3}	730
Water	1.01×10^{-6}	1.01×10^{-3}	998.2
Gas	1.48×10^{-5}	1.79×10^{-5}	1.225

The numerical calculation process is based on the ANSYS commercial software. The pressure implicit split operator (PISO) algorithm is used to deal with pressure–velocity coupling and ensure convergence efficiency [38–40]. The pressure staggering option (PRESTO) solves the pressure discretization interpolation problem [41,42]. The level set function is the Hamilton–Jacobi equation. It is discretized in the fifth-order weighted essentially non-oscillatory (WENO) format in space and the third-order total variation diminishing (TVD) Longo-Kutta format in time [43–45]. In addition, the second-order windward format is used to discretize the momentum and turbulent kinetic energy.

4. Numerical Simulation Results

4.1. Multiphase Vortex Evolution Process

Multiphase vortex is a complex turbulent mechanics phenomenon. Due to the variation of suction force, the interface evolution law takes on highly nonlinear characteristics. In this section, a volume fraction profile is selected to study the dynamic evolution of a multiphase vortex, as shown in Figure 2, where the green region is the water phase, the pink region is the oil phase, and the purple region is the air phase. The figure shows that with the initial disturbance velocity driving, the liquid level near the wall rises, and the center of the free-liquid surface depresses and forms a multiphase-coupling phenomenon.
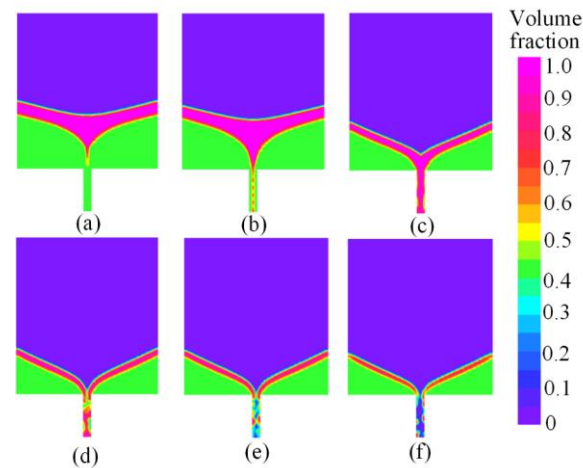

Figure 2. Volume fraction cloud profiles of the multiphase vortex. (**a**) t = 15.0 s, (**b**) t = 18.5 s, (**c**) t = 38.0 s, (**d**) t = 43.5 s, (**e**) t = 46.50 s, (**f**) t = 53.0 s.

In Figure 2a, the multiphase vortex is formed under gravity and initial velocity. The turbulence intensity of the flow field increases, and the water phase is mainly in the drainage pipe. In Figure 2b,c, the vortex scale keeps increasing, the interface becomes a V-shaped opening, and the pipe's interior is mainly water–oil two-phase flow. As oil and water flow from the pipe, the outlet suction promotes the fluid's convergence. A small amount of air is pumped by the drainage outlet, as shown in Figure 2d. The strong suction force effect can overcome the viscous resistance of the fluid and break the energy barrier at the interface center. In Figure 2e, the multiphase fluid at the outlet is unstable, and the fluid composition is a mixture of water, oil, and air. When the flow field forms an air column connected to the outlet atmosphere, the fluid velocities are zero, as shown in Figure 2f. Multiphase vortex in the formation process has a fluid-composition transition, and the flow state and vibration generation are intrinsically linked to the fluid-composition change. The fluid-composition change will affect product quality and production efficiency and is significant for the metallurgical pouring process, chemical process extraction, and other industrial production processes.

To explore the vortex flow field law, the vorticity distribution cloud diagram is obtained, as shown in Figure 3. It can be seen that the vorticity intensity is more significant due to the flow velocity inside the drainpipe. In Figure 3a,b, the vorticity is smaller at the free-liquid surface. The fluid microclusters on the surface have characteristic perturbation patterns at different times and spaces, resulting in fluid microclusters with different velocity gradients along the radial direction. However, in the central region of the vortex, the vorticity values are larger. In Figure 3c,d, the velocity of the vortex surface increases as the vortex evolves, and the vorticity continues to increase in the region above the surface and pipe. The turbulent kinetic energy reaches a maximum, and the rapid macroscopic mixing of turbulent vortices promotes high transport efficiency of turbulent mass, momentum, and energy. In Figure 3e,f, the vorticity distribution does not change significantly, indicating that the flow field has a maximum value in the complex water–oil–gas coupled flow process. If the

vortex formation is to be suppressed, it must be carried out before the multiphase-coupling process, which is of great significance in guiding the vortex-suppression control.
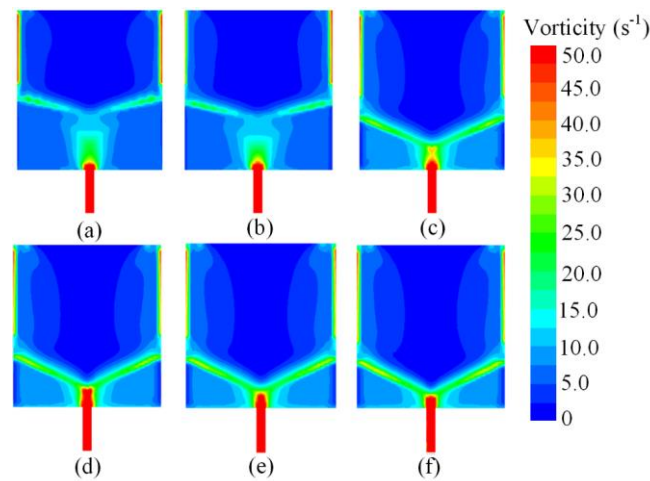

Figure 3. Vorticity cloud profiles of the multiphase vortex. (**a**) t = 15.0 s, (**b**) t = 18.5 s, (**c**) t = 38.0 s, (**d**) t = 43.5 s, (**e**) t = 46.50 s, (**f**) t = 53.0 s.

4.2. Effect of Initial Disturbance Velocity on Vortex

Figure 4 shows the level height of the vortex critical formation state under different initial perturbations. The figure shows that the flow field is in dynamic equilibrium, and the liquid-level height of the water and oil phases increases with the initial disturbance velocity, tending to increase linearly. However, the difference in liquid height between the oil and water phases does not increase linearly. When the initial disturbance is minor, both the early and middle of the drainage process are mainly a single water-phase fluid, so the oil phase still maintains a high share. However, in the late stage, the water- and oil-phase fluids flow out from the orifice together, the process is delayed when the disturbance is low, and the share of the water phase in the early stage decreases faster. Hence, the liquid-level difference between the water and oil phases is larger during the vortex critical formation state. As the initial perturbation speed increases, the centrifugal force on the fluid in the container increases, and the fluid can reach the critical penetration state quickly. At this time, the container's overall share of water and oil is still at a high level, and the level difference is relatively small.
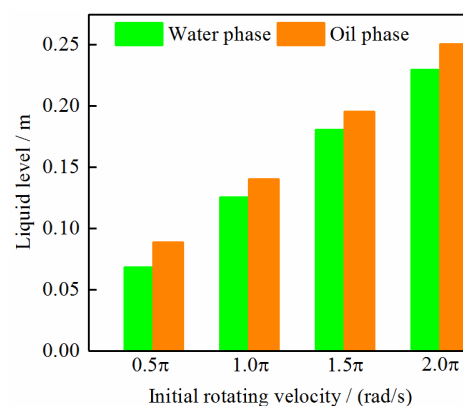

Figure 4. Liquid height at the vortex critical penetration state.

Figure 5 depicts the evolution of the total pressure in the flow field with the draining process. It can be seen from the figure that the changing trend of the total pressure under different initial disturbance velocities is the same. At the early stage of the drain, the pressure curve decreases rapidly with the volume fraction decrease in water and oil phases,

and the drain is the water phase. In the middle of the drain, the total pressure curve decreases continuously, the decline rate decreases slightly, and the drain is water–oil two-phase fluid. The mixing density is less than the pure water phase. In the late stage of the drain, the pressure shows an oscillation phenomenon, the draining process is a complex water–oil–gas coupling state, and the flow rate is unstable. With the increase in the initial disturbance speed, the pressure curve becomes steeper and steeper, and the vortex has a faster energy accumulation and release rate in the late stage of the drain. As drain time decreases, the upper air phase can penetrate the pipe quickly, resulting in complex pressure oscillation. The above laws can provide helpful guidance for the suppression control of vortex-induced vibration.
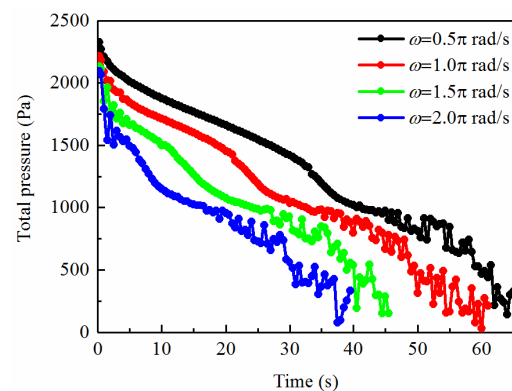

Figure 5. Total pressure variation curves at the whole drain process.

4.3. Generation Mechanism of Fluid-Structure Coupling Vibration

In order to reveal the vortex-induced vibration mechanism, the time-domain waveform of the vibration signal is analyzed as shown in Figure 6, where the horizontal coordinate is the sampling point N, and the vertical coordinate is the vibration amplitude A_t. In Figure 6a, it can be seen that when the pipe is in a single aqueous-phase fluid state, the intensity of the vibration signal is weak, the amplitude ranges from -0.002×10^{-3} m·s^{-2} to -0.002×10^{-3} m·s^{-2}, and there are many nonlinear pulse components. In Figure 6b, when the oil phase is mixed with the water phase, the vibration signal shows prominent pulse components at the sampling point $N = 520$, and the vibration amplitude is 0.028×10^{-3} m·s^{-2}. Then, the vibration signal decreases, indicating that the water and oil phases flow out from the pipe evenly. However, the amplitude of the vibration signal suddenly increases at $N = 1000$, indicating that the flow state changes at this time, and a small amount of gas and oil–water phases begin to mix.

In Figure 6c, the amplitude of the vibration signal increases and reaches the maximum value at some point. In this process, the vibration signal morphology presents nonlinear characteristics due to the mixed transport of water, oil, and gas. The amount of gas increases and mixes with water and oil, forming a complex multiphase flow coupling pattern, and its amplitude is -0.02×10^{-3} m·s^{-2}~-0.02×10^{-3} m·s^{-2}. Compared with the single water-phase flow, the amplitude of the vibration signal is increased by ten times. The peak value of the vibration signal at $N = 980$ can reach 0.43×10^{-3} m·s^{-2}. This characteristic is consistent with the vortex critically penetrating the drain pipe. In Figure 6d, the amplitude of the vibration signal decreases when it is a single air phase, but a small amount of impulse component is present. Based on the time-domain waveform, it can be inferred that there are a series of random shock vibration components in the multiphase-mixing process. The signal has a transient sudden-change characteristic with the maximum amplitude in the critical penetration state. According to this amplitude characteristic, the formation time point of the vortex can be detected using a vibration sensor, which is important for active control of vortex in engineering.
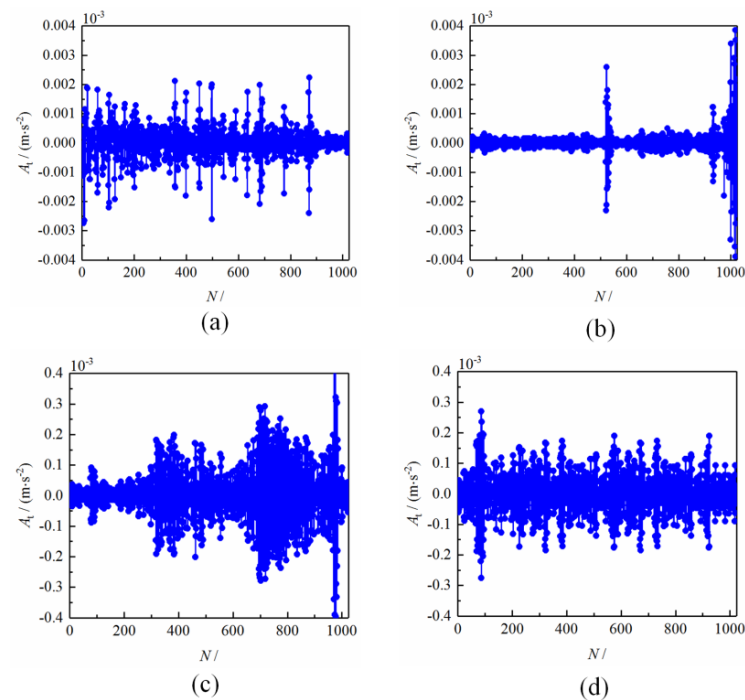
Figure 6. Time-domain characteristics of the vibration signal. (**a**) Single water phase, (**b**) Oil–water two-phase, (**c**) Gas–oil–water mixing phase, (**d**) Single gas phase.

Although the time-domain characteristics can predict the vortex critical formation state, in practical engineering applications, various noise interferences can affect the time-domain waveform profile, resulting in the original accuracy loss of results. The frequency spectrum is the coordinate axis that converts the dynamic signal into frequency by Fourier transform, and the frequency distribution is used to describe the amplitude distribution of the signal. Figure 7 shows the vibration signal spectrum in different flow states, where the horizontal coordinate is the frequency and the vertical coordinate is the amplitude. In Figure 7a,b, when the pipeline flows in a single water phase and oil–water two-phase trend, the frequency amplitude of the signal is 1.62×10^{-7} m·s^{-2}. In Figure 7b, when the pipe is mixed with water and oil, the vibration signal's frequency amplitude increases, decreases, and increases in the range of 35~45 Hz. In Figure 7c, when the pipeline is mixed with water–oil–gas flow mode, the spectrum structure has no prominent feature, and the frequency amplitude increases significantly, reaching a peak of 5×10^{-5} m·s^{-2} at 49.8 Hz. The intense vibration pulse component is generated under the above mixed flow mode. In Figure 7d, the frequency amplitude of the vibration signal decreases, and the frequency amplitude is smaller, from 0 to 40 Hz. Still, the amplitude increases from 45 to 50 Hz, and there are a certain amount of random pulse components. From the above characteristics, it can be seen that the frequency amplitude in the multiphase-mixing process is much larger than that of the single water-phase and water–oil two-phase flow states, and the increment of the frequency amplitude is concentrated in the range of 45~50 Hz. Therefore, the above combined characteristics can be used as the key to the identification of the vortex multiphase coupled flow state.

In the vortex-formation process, the frequency components of the vibration signal have time-varying characteristics. The pipeline is excited by the random signal, and the vibration signal's simple time and frequency-domain analysis cannot obtain the local information of both time and frequency domains [46–48]. The joint time–frequency analysis can better analyze the evolution of frequency and energy of the shock vibration signal with time. It can visually describe the vibration energy evolution of the vortex formation process. Figure 8 shows the three-dimensional time–frequency spectra of the vibration signal under different flow states. From the figure, it can be seen that the frequency range of the vibration signal is concentrated in the range of 30~50 Hz. In Figure 8a,b, the spectral structures of the

vibration signals differ significantly. The former has a series of wave peaks, and the latter has fewer wave peaks. In Figure 8c, the wave peaks of the vibration signal reach their peak near the sampling point $N = 1000$, and the frequencies are mainly concentrated in the range of 30~50 Hz. It indicates that the pulse components generated by the multiphase-mixed flow mode are concentrated in the high-frequency band, which is closely related to the vortex critical penetration moment. In Figure 8d, the signal has uniform peaks, and the amplitude decreases compared with the multiphase-mixed state. Therefore, the waveform and peak at 30 to 50 Hz can be critical for vortex multiphase-mixed flow pattern detection.
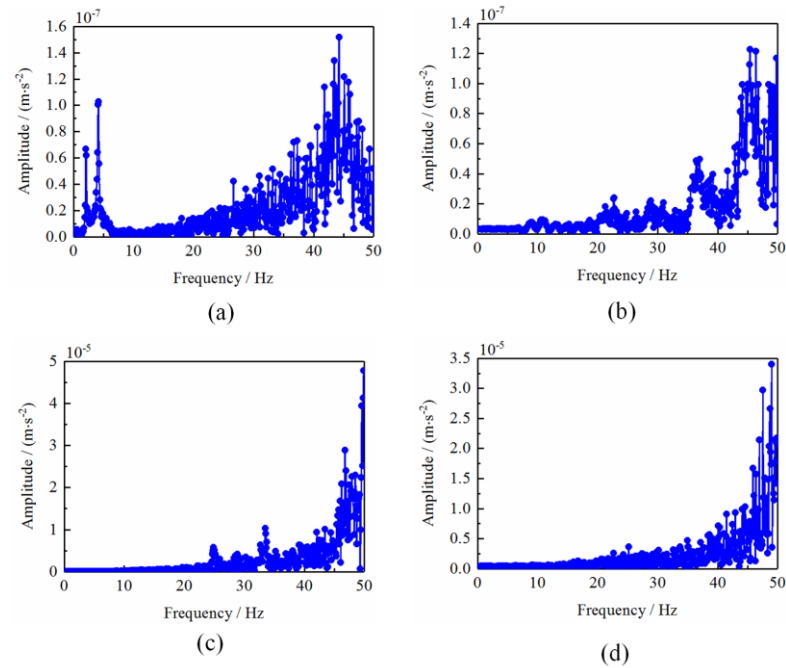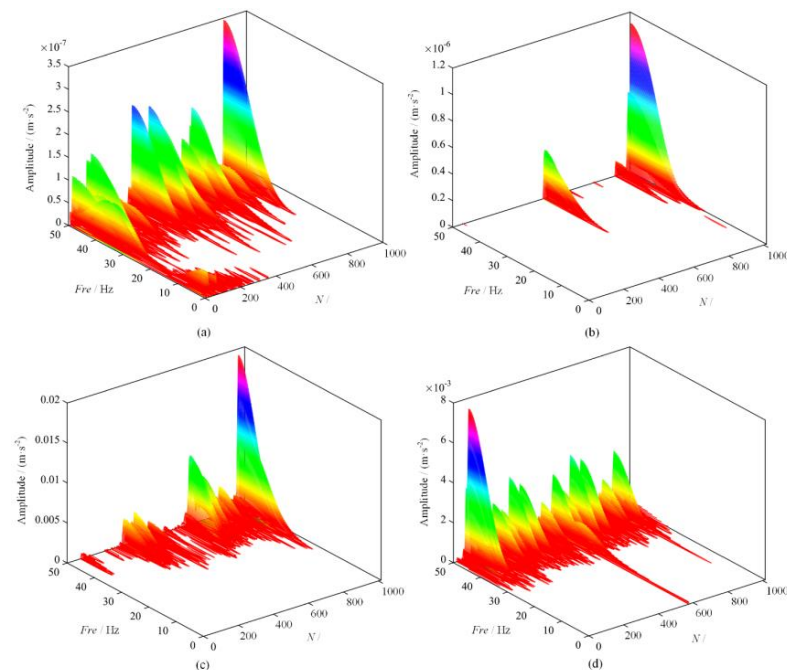

Figure 7. Frequency spectrum characteristics of the vibration signal. (**a**) Single water phase, (**b**) Oil–water two-phase, (**c**) Gas–oil–water mixing phase, (**d**) Single gas phase.

Figure 8. Time/frequency spectrum characteristics of the vibration signal. (**a**) Single water phase, (**b**) Oil–water two-phase, (**c**) Gas–oil–water mixing phase, (**d**) Single gas phase.

5. Multiphase Vortex-Induced Vibration Observation Experiment

5.1. Experimental Platform Construction

Based on the principle of the vibration detection method, a multiphase vortex-induced vibration experimental platform is designed to realize the vibration signal-detection process, as shown in Figure 9. The vibration signal acquisition consists of a target position module, a constant current adapter, a vibration sensor, and a two-core cable. A piezoelectric acceleration sensor with a built-in integrated circuit is selected to measure the vibration of the fluid impinging on the pipe. The sensor base is fixed by a threaded connection to avoid damage to the internal inductive devices, and the sensor base is bonded to the wall of the drainpipe and the experimental bench. Since the piezoelectric sensor has a high input impedance, the two-core cable's relatively weak charge signal is collected during vortex shock. The high-impedance output signal is converted to a low-impedance output signal by gain amplification with a constant current adapter.
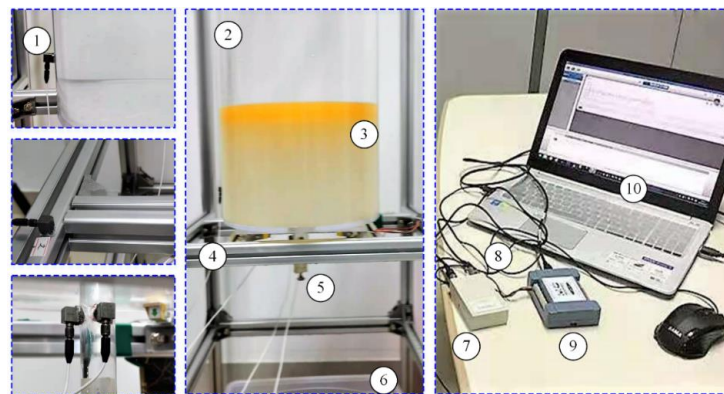

Figure 9. Vibration detection experiment platform of the multiphase vortex. 1—Vibration sensor, 2—Transparent cylindrical container, 3—Two-phase fluid medium, 4—Aluminum test bench, 5—Adjustable throttle, 6—Rectangular overflow container, 7—Constant current adapter, 8—Dual core cable, 9—Data acquisition card, 10—PC control system.

In the water model experiment, the industrial PC sends signals to control the T-agitator and provides a certain initial disturbance speed of the flow field. Then, the stirring is stopped, and the drain port is opened. At this time, the signal acquisition device and the draining process of the container are carried out synchronously. As the fluid impacts the pipeline, the vibration sensor receives the fluid-induced signal and transmits it to the constant current adapter through the signal line. The signal transmits to the PC control end after amplification, filtering, sampling, and A/D conversion, and carries out real-time processing, display, and storage of the vibration signal. When the vibration signal mutates, the PC control end sends the control signal to close the pipe port, and sends the alarm signal at the same time.

5.2. Experimental Vibration Characteristics

Figure 10 depicts a typical time series of the experimental time-domain waveform. The horizontal coordinate is the sampling point N, the vertical coordinate is the vibration amplitude A_t, and the sampling frequency is 100 Hz. Analyzing the time-domain waveform of the vibration signal, the simple harmonic component, the periodic component, or the transient pulse component contained in the time-domain waveform signal can be obtained.
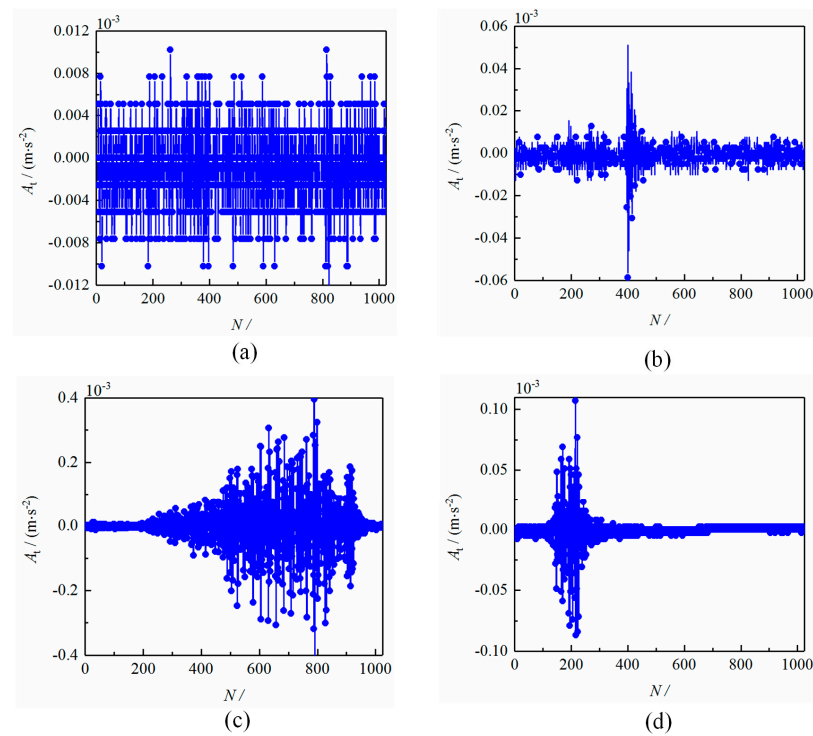
Figure 10. Experimental time-domain characteristics of the vibration signal. (**a**) Single water phase, (**b**) Oil–water two-phase, (**c**) Gas–oil–water mixing phase, (**d**) Single gas phase.

Figure 10a shows the time-domain waveform from a single water phase. The time-domain waveform has a series of uniform pulse components at the initial disturbance velocity. It is indicated that the radial impact force components of the single fluid in the drainpipe do not cause sudden changes in the vibration amplitude. With the stabilization of the vortex flow field, the amplitude of the vibration signal is concentrated in the interval of $-0.006\sim0.006$ m·s^{-3}. Figure 10b shows the time-domain waveform of the signal when the two phases are mixed in the draining process. There is an abrupt peak change, and the peak is in the amplitude range of $-0.06\sim0.05$ m·s^{-3}, related to mixing the oil phase with the water phase in the drainpipe. Figure 10c shows the time-domain waveform of the multiphase-mixed fluid in the draining process. The maximum of the signal amplitude can be reach 0.4×10^{-3} m·s^{-2}, which is in agreement with the numerical results in Figure 6. It can be seen that the amplitude of the vibration signal increases continuously and has a highly nonlinear characteristic. The time-domain structure of the signal is consistent with the numerical results. This nonlinear pulse component is related to the irregular scale and random quantity of the pumping bubbles, which induces the complex multiphase coupled pressure pulsation phenomenon. In Figure 10d, the signal amplitude has apparent decreasing, which is agree with the numerical results in Figure 6d.

The variance of a vibration signal can reflect the varying degree of the signal around the mean value, i.e., it indicates the degree of fluctuation of a signal [49,50]. The variance of four vibration signals with different drain states is processed based on the above time-domain waveform. If the continuous vibration signal is $x(t)$, and the discrete vibration data series as $\{x_{n} \mid n = 1, 2, 3, \ldots, N\}$, then the variance of the signal is

$$\sigma_x = \left(\frac{1}{n} \sum_{i=1}^{n} (x_i - \overline{x})^2 \right)^{\frac{1}{2}} \tag{12}$$

where $\overline{x}$ is the mean value of the discrete vibration data.

The variance of each vibration signal sample data is calculated based on the above time-domain waveform. The results are shown in Figure 11, where the horizontal axis

is the sampling point number N, and the vertical axis is the variance value of vibration signal A_t. From the figure, it can be seen that the variance signals in Figure 11b,c have prominent abrupt change characteristics, and the sudden change in time point corresponds to both the fluid state from single to two-phase mixing and multiphase-coupling state with bubble pumping. The signal variance in Figure 11c has a series of random pulse components and an apparent abrupt peak. It is indicated that the coupling energy shock causes the shell deformation to increase, enhancing nonlinear shock-pulse components and causing the violent vibration phenomenon. The subsequent disappearance of the signal pulse components indicates that the gas phase has penetrated the drainpipe.
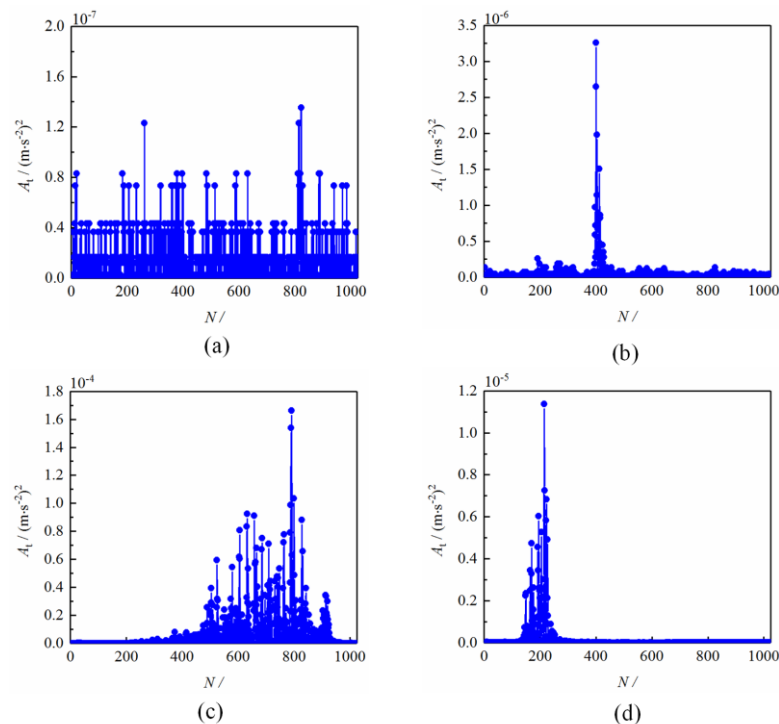

Figure 11. Variance analysis diagrams of different drain states. (**a**) Single water phase, (**b**) Oil–water two-phase, (**c**) Gas–oil–water mixing phase, (**d**) Single gas phase.

According to the time-domain waveform, the vibration signal has randomness during multiphase coupling, and it is impossible to find the internal law. Hence, the frequency spectrum power or amplitude spectrum is widely used for online detection. Figure 12 shows the power spectrum analysis of the vibration signal. The horizontal axis is the sampling frequency *Fre,* and the vertical axis is the power spectrum density A_p. Figure 12a shows the power spectrum of a single fluid. The spectrum amplitude increases in 10~20 Hz and 45~50 Hz. The latter characteristics are in agreement with the numerical results in Figure 7a. Figure 12b shows the power spectrum of the two-phase fluid. It can be seen that the critical transition of the flow state has a certain effect on the amplitude increase, but the effect on the spectral structure is insignificant. Figure 12c shows the power spectrum of multiphase fluids. The coupling energy diffusion causes a significant increase in the range of 40~50 Hz, and the randomness of the frequency distribution in the high-frequency band is enhanced. Figure 12d shows the power spectrum of a single gas fluid. It has a significantly reduced frequency amplitude compared with the former. However, the spectral structure changes significantly, and is related to the vibration energy wave of the fluid-impacting shell after the vortex penetration.
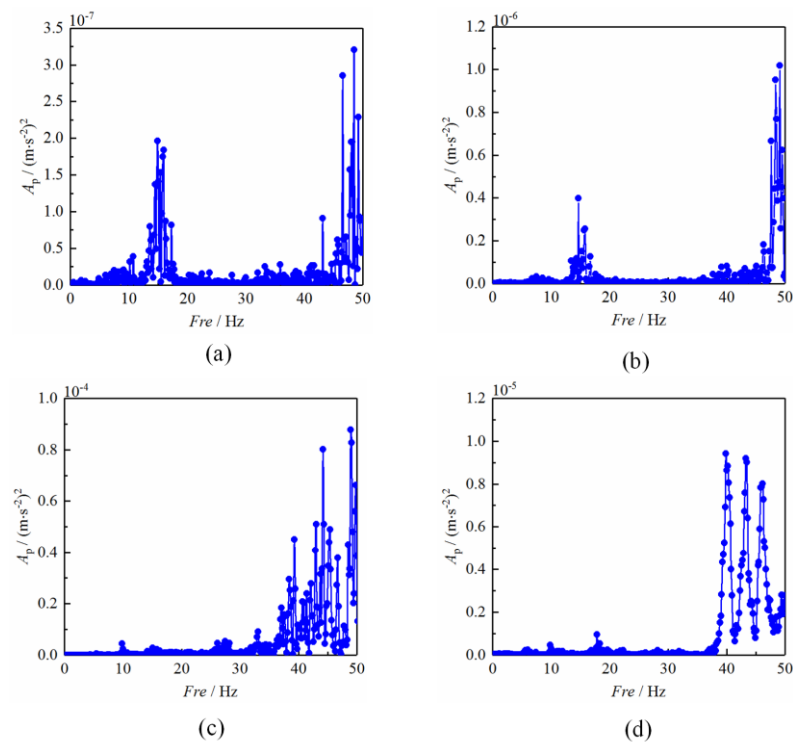
Figure 12. Power spectrum under different drainage states. (**a**) Single water phase, (**b**) Oil–water two-phase, (**c**) Gas–oil–water mixing phase, (**d**) Single gas phase.

From the whole drain process, the multiphase fluid flowing from the pipe needs to go through four stages: single water phase, water–oil two-phase mixing, multiphase fluid mixing, and single gas phase. The amplitude of the vibration signal exists in the process of increasing to the peak, and then decreasing instantaneously. There is a significant change in the frequency amplitude and structure in the high-frequency range of 40~50 Hz. During the multiphase coupling in Figure 12c, the frequency of the vibration signal decreases significantly at 48 Hz, leading to a complex nonlinear characteristic of the structure in the frequency spectrum from 40 to 50 Hz. However, the nonlinear pulse component of the vibration signal under fluid impact decreases significantly after the multiphase fluid penetrates the pipe.

6. Conclusions

The investigation on multiphase vortex-induced vibration has essential scientific research value and engineering application prospects. In this paper, a fluid-structure coupling vibration modeling method is proposed to reveal the vortex-induced vibration evolution mechanism. The main conclusions are as follows:

(1) A multiphase vortex dynamics model is set up to obtain the evolution laws of the vortex formation. The vortex formation has two critical transitions, which induce the single flow to change into a two-phase flow and multiphase flow. The vorticity values in the central region are larger and the energy shock wave in the coupling process causes pressure oscillation.

(2) The frequency amplitude in the multiphase-mixing process is much larger than that of the single water-phase and water–oil two-phase flow state. In the critical penetrating state, the signal has transient distortion characteristics with the largest amplitude. The vibration signal has a high amplitude frequency component in 45~50 Hz, resulting in a highly nonlinear frequency structure.

(3) The different density of fluid medium leads to randomness and nonlinear impact vibration. The amplitude of the vibration signal exists in the process of increasing to the peak, and then decreasing instantaneously. The vibration amplitude of the

45~50 Hz high-frequency band increases obviously, which is related to the large deformation caused by the fluid energy impact on the shell and the sharp noise caused by gas-phase suction during the critical transition. The frequency range of 45~50 Hz amplitude and structure evolution can be used to detect the critical vortex time.

Author Contributions: Conceptualization, G.Z., J.S. and W.X.; article identification, screening, retrieval, selection and analysis, G.Z. and L.L.; formal analysis and investigation, G.Z. and Z.G.; writing—original draft preparation, G.Z. and L.L.; tables and figures generation, G.Z. and B.L.; review and editing, G.Z., J.S., Q.L., W.X., C.W. and Z.G.; supervision, L.L. funding acquisition, L.L. All authors have read and agreed to the published version of the manuscript.

Institutional Review Board Statement: Not applicable.

Informed Consent Statement: Not applicable.

Data Availability Statement: Not applicable.

Conflicts of Interest: The authors declare that they have no conflict of interest.

References

1. Li, L.; Tan, D.P.; Yin, Z.C.; Wang, T.; Fan, X.H.; Wang, R.H. Investigation on the multiphase vortex and its fluid-solid vibration characters for sustainability production. *Renew. Energy* **2021**, *175*, 887–909. [CrossRef]
2. Li, L.; Tan, D.P.; Wang, T.; Yin, Z.C.; Fan, X.H.; Wang, R.H. Multiphase coupling mechanism of free surface vortex and the vibration-based sensing method. *Energy* **2021**, *216*, 119136. [CrossRef]
3. Ni, D.; Zhang, N.; Gao, B.; Li, Z.; Yang, M.G. Dynamic measurements on unsteady pressure pulsations and flow distributions in a nuclear reactor coolant pump. *Energy* **2020**, *198*, 117305. [CrossRef]
4. Tan, D.P.; Zhang, L.B. A WP-based nonlinear vibration sensing method for invisible liquid steel slag detection. *Sens. Actuators B* **2014**, *202*, 1257–1269. [CrossRef]
5. Li, L.; Qi, H.; Yin, Z.C.; Li, D.F.; Zhu, Z.L.; Tangwarodomnukun, V.; Tan, D.P. Investigation on the multiphase sink vortex Ekman pumping effects by CFD-DEM coupling method. *Powder Technol.* **2020**, *360*, 462–480. [CrossRef]
6. Tan, D.P.; Li, L.; Yin, Z.C.; Li, D.F.; Zhu, Y.L.; Zheng, S. Ekman boundary layer mass transfer mechanism of free sink vortex. *Int. J. Heat Mass Transfer.* **2020**, *150*, 119250. [CrossRef]
7. Sun, Z.; Jin, H.; Gu, J. Studies on the online intelligent diagnosis method of undercharging sub-health air source heat pump water heater. *Appl. Therm. Eng.* **2020**, *169*, 114957. [CrossRef]
8. Tan, D.P.; Li, P.Y.; Ji, Y.X.; Wen, D.H.; Li, C. SA–ANN–based slag carry-over detection method and the embedded WME platform. *IEEE Trans. Ind. Electron.* **2013**, *60*, 4702–4713. [CrossRef]
9. Li, L.; Lu, B.; Xu, W.X.; Gu, Z.H.; Yang, Y.S.; Tan, D.P. Mechanism of multiphase coupling transport evolution of free sink vortex. *Acta Phys. Sin.* **2023**, *72*, 034702. [CrossRef]
10. Son, J.H.; Sohn, C.H.; Park, I.S. Numerical study of 3-D air core phenomenon during liquid draining. J. *Mech. Sci. Technol.* **2015**, *29*, 4247–4257. [CrossRef]
11. Tan, D.P.; Li, L.; Zhu, Y.L.; Zheng, S.; Yin, Z.C.; Li, D.F. Critical penetration condition and Ekman suction-extraction mechanism of a sink vortex. J. *Zhejiang Univ.-Sci. A* **2019**, *20*, 61–72. [CrossRef]
12. Kim, D.; Kim, D. Free-surface vortex formation and aeration by a submerged rotating disk. *Chem. Eng. Sci.* **2021**, *243*, 116787. [CrossRef]
13. Ahn, S.H.; Xiao, Y.X.; Wang, Z.W.; Zhou, X.Z.; Luo, Y.Y. Numerical prediction on the effect of free surface vortex on intake flow characteristics for tidal power station. *Renew. Energy* **2017**, *101*, 617–628. [CrossRef]
14. Takacs, G.; Ondrejkovic, K.; Hulko, G. A low-cost non-invasive slag detection system for continuous casting. *IFAC Pap.* **2017**, *50*, 438–445. [CrossRef]
15. Wang, Q.; Wang, L.Y.; Li, H.X.; Jiang, J.W.; Zhu, X.W.; Guo, Z.C.; He, J.C. Suppression mechanism and method of vortex during steel teeming process in ladle. *Acta Metall. Sin.* **2018**, *7*, 959–968.
16. Zhang, Q.; Wang, J.; Zhang, Y.Z.; Xu, G.G. Numerical simulation and manifold learning for the vibration of molten steel draining from a ladle. J. *Vibroeng.* **2013**, *15*, 549–557.
17. Li, S.; Chen, R.; Wang, H. Numerical investigation of the moving liquid column coalescing with a droplet in triangular microchannels using CLSVOF method. *Sci. Bull.* **2015**, *60*, 1911–1926. [CrossRef]
18. Tan, D.P.; Ni, Y.S.; Zhang, L.B. Two-phase sink vortex suction mechanism and penetration dynamic characteristics in ladle teeming process. J. *Iron Steel Res. Int.* **2017**, *24*, 669–677. [CrossRef]

19. Li, L.; Lu, J.; Fang, H.; Yin, Z.; Wang, T.; Wang, R.; Fan, X.; Zhao, L.; Tan, D.; Wan, Y. Lattice Boltzmann method for fluid-thermal systems: Status, hotspots, trends and outlook. *IEEE Access* **2020**, *8*, 27649–27675. [CrossRef]

20. Ni, Y.S.; Tan, Y.F.; Tan, D.P. Multi-physical modeling and adjusting for ultrasonic assisted soft abrasive flow processing. *Chin. J. Mech. Eng.* **2023**, in press. [CrossRef]

21. Zheng, M.R.; Han, D.; Peng, T. Numerical investigation on flow induced vibration performance of flow-around structures with different angles of attack. *Energy* **2022**, *244*, 122607. [CrossRef]

22. Cristofano, L.; Nobili, M.; Romano, G.P.; Caruso, G. Investigation on bathtub vortex flow field by particle image velocimetry. *Exp. Therm. Fluid Sci.* **2016**, *74*, 130–142. [CrossRef]

23. Li, L.; Xu, W.X.; Tan, Y.F.; Yang, Y.S.; Yang, J.G.; Tan, D.P. Fluid-induced vibration evolution mechanism of multiphase free sink vortex and the multi-source vibration sensing method. *Mech. Syst. Signal Process.* **2023**, *189*, 110058. [CrossRef]

24. Auguste, C.; Nader, J.R.; Marsh, P. Modelling the influence of Tidal Energy Converters on sediment dynamics in Banks Strait, Tasmania. *Renew. Energy* **2022**, *188*, 1105–1119. [CrossRef]

25. Tan, Y.F.; Ni, Y.S.; Wu, J.F.; Li, L.; Tan, D.P. Machinability evolution of gas-liquid-solid three-phase rotary abrasive flow finishing. *Int. J. Adv. Manuf. Technol.* **2023**, in press. [CrossRef]

26. Wang, J.X.; Gao, S.B.; Tang, Z.J.; Tan, D.P.; Cao, B.; Fan, J. A context-aware recommendation system for improving manufacturing process modeling. *J. Intell. Manuf.* **2021**, in press. [CrossRef]

27. Zhao, K.Q.; Fan, J.; Wang, B. Analytical and experimental study of the vibro-acoustic behavior of a semi -submerged finite cylindrical shell. *J. Sound Vib.* **2020**, *482*, 115466. [CrossRef]

28. Zheng, G.A.; Gu, Z.H.; Xu, W.X.; Li, Q.H.; Tan, Y.F.; Wang, C.Y.; Li, L. Gravitational surface vortex formation and suppression control: A review from hydrodynamic characteristics. *Processes* **2023**, *11*, 42. [CrossRef]

29. Li, Q.; Ouyang, J.; Yang, B.X.; Jiang, T. Modelling and simulation of moving interfaces in gas-assisted injection moulding process. *Appl. Math. Model.* **2011**, *35*, 257–275. [CrossRef]

30. Zhou, Z.Y.; Qin, W.Y.; Zhu, P.; Du, W.F. Harvesting more energy from variable-speed wind by a multi-stable configuration with vortex-induced vibration and galloping. *Energy* **2021**, *237*, 121551. [CrossRef]

31. Sun, L.Y.; Pan, Q.; Zhang, D.S. Numerical study of the energy loss in the bulb tubular pump system focusing on the off-design conditions based on combined energy analysis methods. *Energy* **2022**, *258*, 124794. [CrossRef]

32. Wang, Y.Y.; Zhang, Y.L.; Tan, D.P.; Zhang, Y.C. Key technologies and development trends in advanced intelligent sawing equipments. *Chin. J. Mech. Eng.* **2021**, *34*, 30. [CrossRef]

33. Li, L.; Gu, Z.H.; Xu, W.X.; Tan, Y.F.; Fan, X.H.; Tan, D.P. Mixing mass transfer mechanism and dynamic control of gas-liquid-solid multiphase flow based on VOF-DEM coupling. *Energy* **2023**, in press.

34. Ge, J.Q.; Ren, Y.L.; Li, C.; Li, Z.A.; Yan, S.T.; Tang, P.; Xu, X.S.; Wang, Q. Ultrasonic coupled abrasive jet polishing (UC-AJP) of glass-based micro-channel for micro-fluidic chip. *Int. J. Mech. Sci.* **2023**, in press. [CrossRef]

35. Li, L.; Tan, Y.F.; Xu, W.X.; Ni, Y.S.; Yang, J.G.; Tan, D.P. Fluid-induced transport dynamics and vibration patterns of multiphase vortex in the critical transition states. *Int. J. Mech. Sci.* **2023**, *189*, 110058.

36. Tan, D.P.; Li, L.; Zhu, Y.L.; Zheng, S.; Ruan, H.J.; Jiang, X.Y. An embedded cloud database service method for distributed industry monitoring. *IEEE Trans. Ind. Inform.* **2018**, *14*, 2881–2893. [CrossRef]

37. Thiebaut, M.; Quillien, N.; Maison, A. Investigating the flow dynamics and turbulence at a tidal-stream energy site in a highly energetic estuary. *Renew. Energy* **2022**, *195*, 252–262. [CrossRef]

38. Tan, D.P.; Ji, S.M.; Fu, Y.Z. An improved soft abrasive flow finishing method based on fluid collision theory. *Int. J. Adv. Manuf. Technol.* **2016**, *85*, 1261–1274. [CrossRef]

39. Yin, Z.C.; Ni, Y.S.; Li, L.; Wang, T.; Wu, J.F.; Li, Z.; Tan, D.P. Numerical modelling and experimental investigation of a two-phase sink vortex and its fluid-solid vibration characteristics. *J. Zhejiang Univ.-Sci. A* **2023**, in press.

40. Li, L.; Li, Q.H.; Ni, Y.S.; Wang, C.Y.; Tan, Y.F.; Tan, D.P. Critical penetrating vibration evolution behaviors of the gas-liquid coupled vortex flow. *Energy* **2023**, in press.

41. Li, L.; Yang, Y.S.; Xu, W.X.; Lu, B.; Gu, Z.H.; Yang, J.G.; Tan, D.P. Advances in the multiphase vortex-induced vibration detection method and its vital technology for sustainable industrial production. *Appl. Sci.* **2022**, *12*, 8538. [CrossRef]

42. Singh, N.K.; Premachandran, B. Coupled level set and volume of fluid method on unstructured grids for the direct numerical simulations of two-phase flows including phase change. *Int. J. Heat Mass Transf.* **2018**, *122*, 182–203. [CrossRef]

43. Yin, Z.C.; Wan, Y.H.; Fang, X.H.; Li, L.; Wang, T.; Wang, Z.; Tan, D.P. Brain-computer interfaces: Trends and outlook. *Appl. Intell.* **2022**, in press.

44. Sun, Z.; Jin, H.; Xu, Y. Severity-insensitive fault diagnosis method for heat pump systems based on improved benchmark model and data scaling strategy. *Energy Build.* **2022**, *256*, 111733. [CrossRef]

45. Wang, T.; Li, L.; Yin, Z.; Xie, Z.; Wu, J.; Zhang, Y.; Tan, D. Investigation on the flow field regulation characteristics of the right-angled channel by impinging disturbance method. *Proc. Inst. Mech. Eng. Part C J. Mech. Eng. Sci.* **2022**, *236*, 11196–11210. [CrossRef]

46. Lv, H.P.; Zhang, L.B.; Tan, D.P.; Fang, X. A collaborative assembly for low-voltage electrical apparatuses. *Front. Inf. Technol. Electron. Eng.* **2021**, in press.

47. Randall, R.B. A history of cepstrum analysis and its application to mechanical problems. *Mech Syst Signal Process* **2017**, *97*, 3–19. [CrossRef]

48. Pons-Llinares, J.; Antonino-Daviu, J.A.; Riera-Guasp, M.; Pineda-Sanchez, M. Induction motor diagnosis based on a transient current analytic wavelet transform via frequency B-splines. *IEEE Trans. Ind. Electron.* **2011**, *58*, 1530–1544. [CrossRef]

49. Li, L.; Lu, B.; Xu, W.X.; Li, Q.H.; Wu, J.F.; Ni, Y.S.; Tan, D.P. Fluid-induced vibration transition behaviors and sensing platform of the multiphase sink vortex. *Energy* **2023**, *189*, 110058.

50. Zhang, L.B.; Lv, H.P.; Tan, D.P.; Fang, X.; Chen, J.L.; Bao, G.J.; Cai, S.B. An adaptive quantum genetic algorithm for task sequence planning of complex assembly systems. *Electron. Lett.* **2018**, *54*, 870–871. [CrossRef]